J. Fluid Mech. (2000), *vol.* 413, *pp.* 65–88. Printed in the United Kingdom

The rate of spreading in spin coating

By S. K. WILSON,† R. HUNT AND B. R. DUFFY

Department of Mathematics, University of Strathclyde, Livingstone Tower, 26 Richmond Street, Glasgow G1 1XH, UK

(Received 1 June 1998 and in revised form 22 December 1999)

In this paper we reconsider the fundamental problem of the centrifugally driven spreading of a thin drop of Newtonian fluid on a uniform solid substrate rotating with constant angular speed when surface-tension and moving-contact-line effects are significant. We discuss analytical solutions to a number of problems in the case of no surface tension and in the asymptotic limit of weak surface tension, as well as numerical solutions in the case of weak but finite surface tension, and compare their predictions for the evolution of the radius of the drop (prior to the onset of instability) with the experimental results of Fraysse & Homsy (1994) and Spaid & Homsy (1997). In particular, we provide a detailed analytical description of the no-surface-tension and weak-surface-tension asymptotic solutions. We demonstrate that, while the asymptotic solutions do indeed capture many of the qualitative features of the experimental results, quantitative agreement for the evolution of the radius of the drop prior to the onset of instability is possible only when weak but finite surface-tension effects are included. Furthermore, we also show that both a fixed- and a specific variable-contact-angle condition (or 'Tanner law') are capable of reproducing the experimental results well.

1. Introduction

Because of the uniformity and thinness of the fluid layers it produces combined with its speed, simplicity and low cost, spin coating (the spreading of a thin film of fluid over a rotating substrate by the action of centrifugal forces) has long been a popular high-volume production technique for advanced electronic devices. In particular, spin coating is used in the microelectronics industry for coating polymer 'resist' layers for photolithographic processing of integrated circuits and for the deposition of inorganic colloidal surface coatings on laser optical components such as highly reflective mirrors (see Larson & Rehg 1997 for further details of practical applications). In practice the substrates can have very complicated geometries and the fluids used are often highly non-Newtonian. However, despite considerable theoretical and experimental progress in recent years there are still several interesting unresolved questions concerning even the simplest situation, namely the spreading of Newtonian fluid on a planar substrate rotating with constant angular velocity.

The pioneering analysis of spin coating was performed more than forty years ago by Emslie, Bonner & Peck (1958), who considered the spreading of a thin axisymmetric film of Newtonian fluid on a planar substrate rotating with constant angular velocity. They obtained the exact solution for the evolution of the film due purely to centrifugal and viscous forces. In particular, this solution shows that

† Author for correspondence: e-mail: s.k.wilson@strath.ac.uk.

initially non-uniform free-surface profiles tend to become increasingly uniform during spinning. Subsequent authors have generalized the work of Emslie *et al.* (1958) to include various additional physical effects, including non-Newtonian fluid behaviour, non-planar substrates, surface roughness, Coriolis effects, fluid inertia, evaporation and adsorption. Larson & Rehg (1997) review this literature.

The experimental studies of Melo, Joanny & Fauve (1989), Fraysse & Homsy (1994) and Spaid & Homsy (1997) (the last two works are hereafter referred to as FH and SH, respectively, for brevity) show that typically the profile of the spreading film rapidly becomes almost flat except near the contact line where a 'capillary ridge' forms. Moreover, the theoretical analysis of the problem in the asymptotic limit of weak surface-tension effects is found to be in qualitative agreement with these observations. This analysis shows that in this limit surface-tension effects are negligible in the 'outer' region away from the contact line and so the evolution of the profile in this region is described by the solution in the absence of surface-tension effects obtained by Emslie *et al.* (1958), while in the 'inner' region in the vicinity of the contact line there is a quasi-static balance between surface tension and centrifugal forces responsible for the formation of the capillary ridge. This description was first proposed by Huppert (1982) for the closely related problem of the gravity-driven draining of a thin, two-dimensional film of viscous fluid down an inclined plane, and the leading-order asymptotic solution in the inner region was first correctly analysed in the seminal paper by Troian *et al.* (1989). The first uniformly valid leading-order composite solutions were obtained by Moriarty, Schwartz & Tuck (1991) who analysed two-dimensional gravity-driven draining and spreading due to an externally applied jet of air, as well as the axisymmetric spin coating problem. In particular, Moriarty *et al.* (1991) obtained excellent agreement between their asymptotic solutions and their own numerical solutions of the governing lubrication equation for certain parameter values corresponding to fairly weak surface tension. The linear stability of the flow in the inner region was first investigated by Troian *et al.* (1989), who showed that it is always unstable to transverse disturbances with sufficiently long wavelength and identified a most unstable wavenumber. The mechanism of this instability has been discussed by Brenner (1993), Spaid & Homsy (1996) and Bertozzi & Brenner (1997).

Experimental investigations of spin coating have been performed by Melo *et al.* (1989), FH and SH. In all three of these papers the authors placed drops of various fluids with various volumes onto a horizontal turntable and then measured the evolution of the drop as it spread. All three observed the same qualitative features, namely that the contact line of the drop initially retains its approximately circular shape as it begins to spread, but at a critical radius (or alternatively at a critical time) the capillary ridge that develops near the contact line becomes unstable and the contact line develops a wavy perturbation which evolves into well-defined 'fingers' which grow and eventually spread to the edge of the turntable (see, for example, figure 1 of Melo *et al.* 1989). Several features of these experiments are in good quantitative agreement with the existing theory. Most notably, the experimentally measured azimuthal wavenumber and growth rates of the instability are in good agreement with the predictions of the linear stability theory of Troian *et al.* (1989) described above, but only provided that the critical radius for the onset of instability (for which there is at present no theoretical prediction) is taken from the experiment itself. However, the evolution of the radius of the drop prior to the onset of instability is not in good agreement with the simple analytical results for a uniform initial profile in the limit of small surface tension with which it has so far been compared (see figure 10 of FH). The main purpose of the present paper is to make a detailed comparison

Experiment	ρ ($g\,cm^{-3}$)	ν ($cm^2\,s^{-1}$)	σ ($dyn\,cm^{-1}$)	ω (s^{-1})	R_0 (mm)	V (μl)
PDMS1	0.97	10	21.2	15.7	7.8	97.5
PDMS2	0.97	10	21.2	31.4	8.1	96.0
PDMS3	0.97	52	21.2	46.9	6.2	88.0
PDMS4	0.97	100	21.2	31.4	5.9	98.0
PDMS5	0.97	100	21.2	62.8	6.1	98.0
TCP1	1.16	0.733	41.0	41.9	7.1	98.0
TCP2	1.16	0.733	41.0	41.9	7.2	97.0

TABLE 1. Values of the fluid density ρ, kinematic viscosity $\nu = \mu/\rho$, surface tension σ, angular velocity of the turntable ω, initial drop radius R_0 and initial drop volume V in the experiments of FH (PDMS) and SH (TCP).

between both analytical and numerical theoretical results and the experimental results of FH and SH for the evolution of the radius of the drop prior to the onset of instability. Of interest in the present work are the experimental runs using Newtonian fluids, specifically the five experiments using polydimethylsiloxane (PDMS) reported by FH (denoted by PDMS1, PDMS2, …, PDMS5) and the two experiments using tricresyl phosphate (TCP) reported by SH (denoted by TCP1 and TCP2). The values of the relevant experimental parameters are summarized in table 1. As we shall demonstrate in the present paper, the leading-order asymptotic solution in the limit of weak surface tension (of which the simple analytical result mentioned above is a special case) is unable to capture accurately the evolution of the radius in any of these experiments. FH show that accounting for the volume of fluid in the capillary ridge (formally neglected in the leading-order asymptotic theory) in an ad hoc manner improves the agreement between theory and experiment. This approach is supported by the numerical results obtained in the present paper for weak but finite surface-tension effects which show good agreement between theory and experiment.

In this paper we reconsider the fundamental problem of the centrifugally driven spreading of a thin drop of Newtonian fluid on a uniform solid substrate rotating with constant angular speed when surface-tension and moving-contact-line effects are significant. We shall discuss analytical solutions to a number of problems in the case of no surface tension and in the asymptotic limit of weak surface tension, as well as numerical solutions in the case of weak but finite surface tension, and we compare their predictions for the evolution of the radius of the drop prior to the onset of instability with the experimental results of FH and SH. In particular, we shall provide a detailed analytical description of the no-surface-tension and weak-surface-tension asymptotic solutions. We shall demonstrate that, while the asymptotic solutions do indeed capture many of the qualitative features of the experimental results, quantitative agreement for the evolution of the radius of the drop prior to the onset of instability is possible only when weak but finite surface-tension effects are included. Furthermore, we shall also show that both a fixed- and a specific variable-contact-angle condition (or 'Tanner law') are capable of reproducing the experimental results well.

2. Problem formulation

Consider a constant volume of incompressible Newtonian fluid with constant viscosity μ and density ρ spreading on a solid horizontal turntable rotating at constant angular speed ω. We investigate the situation in which the flow is axisymmetric about the axis of rotation of the turntable and, using the natural polar coordinates (r, θ, z), write the thickness of the fluid film as $h = h(r, t)$, where t denotes time. We assume that the fluid film is sufficiently slender (and, in particular, that the contact angle is sufficiently small) that we can make the familiar lubrication approximation to the governing Navier–Stokes equations. At the free surface of the film, $z = h(r, t)$, the usual boundary conditions hold, namely the kinematic condition together with the conditions of no tangential stress and of a normal-stress jump equal to the constant coefficient of surface tension σ times the mean curvature of the surface. The air above the drop is assumed to be at constant ambient pressure. In order to mitigate the familiar stress singularity that would otherwise occur at the contact line we impose the ad hoc slip condition $u = \lambda u_z/3$ at the solid substrate, $z = 0$, where u is the radial component of velocity and $\lambda = \lambda(h)$ is a slip length. Several different models have been proposed for λ; here we shall consider the two simplest, namely the classical slip model proposed by Navier (see, for example, Hocking 1983) in which $\lambda = \beta_N$, where β_N is a positive constant with dimensions of length, and the slip model proposed by Greenspan (1978) in which $\lambda = \beta_G/h$, where β_G is a positive constant with dimensions of length squared. The position of the three-phase contact line where $h = 0$ is denoted by $r = R(t)$, and the contact angle is given by $\theta(t) = -h_r$ evaluated at $r = R$.

The thickness of the fluid film is governed by the mass conservation equation

$$h_t + \frac{1}{r}(rQ)_r = 0, \tag{1}$$

where Q denotes the volume flux per unit circumference. Provided that the rotation speed is sufficiently large that gravity effects may be neglected, but sufficiently small that acceleration in the inertial frame rotating with the turntable and the Coriolis force may also be neglected (these conditions are made explicit subsequently) then the only significant inertial effect is the centrifugal force, and Q is given by

$$Q = \int_0^h u \,\mathrm{d}z = \frac{h^2(h+\lambda)}{3\mu}\left[\sigma\left(\frac{(rh_r)_r}{r}\right)_r + \rho\omega^2 r\right]. \tag{2}$$

In addition to an appropriate initial condition, (1) is to be solved subject to two regularity conditions at $r = 0$ and a global volume-conservation condition which requires that the total volume of fluid, V, is constant. Note that (1) is an expression of *local* conservation of volume. The presence of the moving contact line means that *global* conservation of volume (or equivalently no mass flux through the contact line) must, in general, be imposed as an additional condition (see, for example, Young 1994).

Equation (1) requires one further boundary condition, and so it is natural to impose a condition at $r = R$ involving the contact angle θ. Several different conditions have been proposed. For example, Greenspan (1978) assumed that the macroscopic contact angle is linearly related to the contact-line speed, and this 'Tanner law' was subsequently generalized to a specific power-law dependence by Ehrhard & Davis (1991). This approach has been applied to the study of a variety of problems involving the dynamics of thin fluid films, including the spreading of a drop (Greenspan 1978), the spreading of a non-isothermal drop (Ehrhard & Davis 1991), the spreading of a pendent drop (Ehrhard 1994), the spreading of a volatile drop (Anderson & Davis 1995), the reactive spreading of a drop (Braun *et al.* 1995), the opening and closing of a hole in a film (Wilson & Terrill 1996; López, Miksis & Bankoff 1997*a*), the non-isothermal draining of a film (López, Bankoff & Miksis 1996), the draining of a film including inertial effects (López, Miksis & Bankoff 1997*b*), the quasi-static stability of a rivulet (Wilson & Duffy 1998) and the quasi-static spreading of a drop during spin coating or under an externally applied jet of air (McKinley, Wilson & Duffy 1999). On the other hand, Hocking (1983) proposed that the microscopic contact angle always takes a constant value equal to the static contact angle, and by adopting the Navier slip model was able to calculate a relationship between the macroscopic contact angle and the contact-line speed. Subsequently Hocking (1994) extended this analysis to include intermolecular forces. Taking a conceptually similar approach, Shikhmurzaev (1997*a, b*) modelled the thermodynamic state of the interfacial regions near the contact line and, by accounting for the relaxation in fluid properties as a fluid element traverses the contact-line zone, was also able to determine a relationship between the macroscopic contact angle and the contact-line speed. The recent review by Oron, Davis & Bankoff (1997) includes a detailed account of the different theoretical treatments of the contact line; in the present work we will consider two of these. First, we will assume that the contact angle is prescribed, that is, we require that

$$\theta = \theta_0, \tag{3}$$

where the constant $\theta_0 = \theta(0) \geqslant 0$ is the initial value of the contact angle. Secondly, we will assume that the relationship between the contact-line speed, R_t, and the contact angle, θ, is given by a Tanner law of the form

$$R_t = \kappa(\theta^3 - \theta_0^3), \tag{4}$$

where again $\theta_0 = \theta(0) \geqslant 0$ is equal to the initial value of the contact angle and $\kappa > 0$ is an empirically determined constant. Theoretical results (see, for example, Hocking 1992 and Duffy & Wilson 1997) suggest that this Tanner law should be appropriate provided that the slip coefficient β is neither too large (in which case the flow would be dominated by slip) nor too small (in which case the contact line would be essentially immobile).

An alternative way to mitigate the singularity at the contact line is to include a thin 'precursor layer' of uniform thickness $\delta = \delta(t)$ which pre-wets the substrate ahead of the drop. This approach removes the contact line explicitly from the problem and so removes the contact-line singularity without invoking a slip coefficient; it has been used by several authors, including Troian *et al.* (1989) and Moriarty *et al.* (1991). The present formulation is easily modified to include a uniform precursor layer and we shall also present results in this case.

We non-dimensionalize the problem using the initial radius $R_0 = R(0)$ as the characteristic horizontal lengthscale, $H_0 = V/\pi R_0^2$ as the characteristic vertical lengthscale, and $T_0 = \mu/\rho\omega^2 H_0^2$ as the characteristic timescale. In particular, θ is scaled with the aspect ratio $A_0 = H_0/R_0$ and λ with H_0. Table 2 shows the values of H_0, T_0, θ_0 and A_0 for the relevant experiments of FH and SH. Note that the static contact angle of the PDMS fluid used by FH is zero and the spreading begins from the *quasi-static* profile that the drop achieves after being deposited on the stationary turntable and left to relax 'for a few minutes'. In the absence of any information about the (slow) variation of this quasi-static contact angle with time we assume that it remains equal to its initial value throughout the spreading process (up to 8 minutes in the longest case reported), i.e. that $\theta_0 = \theta(0)$ can indeed be treated as a constant in (3) and (4). The TCP fluid used by SH has a non-zero static contact angle and consequently no similar uncertainty arises in this case.

Written in terms of appropriate non-dimensional variables (used hereafter unless

Experiment	H_0 (mm)	T_0 (s)	θ_0	A_0	$1/Fr$	Re	ϵ
PDMS1	0.510	15.58	0.262	0.0654	0.3334	1.67×10^{-5}	0.230
PDMS2	0.466	4.67	0.230	0.0575	0.0706	4.64×10^{-5}	0.134
PDMS3	0.729	4.45	0.470	0.1175	0.0845	2.30×10^{-5}	0.170
PDMS4	0.896	12.62	0.608	0.1519	0.2559	6.36×10^{-6}	0.254
PDMS5	0.838	3.60	0.550	0.1374	0.0560	1.95×10^{-5}	0.150
TCP1	0.619	0.109	0.349	0.0872	0.0686	0.048	0.170
TCP2	0.596	0.118	0.331	0.0827	0.0642	0.041	0.165

TABLE 2. Values of the parameters $H_0 = V/\pi R_0^2$, $T_0 = \mu\pi^2 R_0^4/\rho\omega^2 V^2$, $\theta_0 = 4V/\pi R_0^3$, $A_0 = H_0/R_0$, $1/Fr = gH_0/R_0^2\omega^2$, $Re = (H_0^2\omega\rho/\mu)^2$ and $\epsilon = (\sigma H_0/\rho\omega^2 R_0^4)^{1/3}$ in the experiments of FH (PDMS) and SH (TCP).

stated otherwise) the governing equation (1) becomes

$$h_t + \frac{1}{3r}\left\{rh^2(h+\lambda)\left[\epsilon^3\left(\frac{(rh_r)_r}{r}\right)_r + r\right]\right\}_r = 0, \tag{5}$$

where the parameter

$$\epsilon^3 = \frac{\sigma H_0}{\rho\omega^2 R_0^4} = \frac{\sigma V}{\pi\rho\omega^2 R_0^6} \tag{6}$$

is the appropriate non-dimensional measure of the ratio of surface-tension and centripetal effects introduced by Moriarty *et al.* (1991). Note that the capillary number $Ca = \rho\omega^2 H_0^2 R_0/\sigma$ used by Troian *et al.* (1989) is related to ϵ by $Ca = (A_0/\epsilon)^3$. Equation (5) is to be solved subject to the initial condition

$$h(r,0) = h_0(r), \tag{7}$$

which satisfies $h_0(1) = 0$ so that $R(0) = 1$, the regularity conditions

$$h_r = 0, \quad h_{rrr} = 0 \tag{8}$$

at $r = 0$, together with

$$h = 0 \tag{9}$$

and

$$h_r = -\theta \tag{10}$$

at the contact line $r = R(t)$, where the contact angle θ satisfies either the fixed-contact-angle condition

$$\theta = \theta_0 \tag{11}$$

or the Tanner law

$$R_t = K(\theta^3 - \theta_0^3), \tag{12}$$

where the parameter $K = \epsilon^3\mu\kappa/\sigma$ is a non-dimensional measure of the speed of the contact line. In addition we impose the global volume-conservation condition

$$2\int_0^R (h-\delta)r\,\mathrm{d}r = 1, \tag{13}$$

where δ is the thickness of any uniform precursor layer.

At least initially, the fluid film is slender provided that $A_0 \ll 1$ (or equivalently

$\epsilon Ca^{1/3} \ll 1$), while gravity effects are negligible if the appropriately defined Froude number, $Fr = R_0^2\omega^2/gH_0$, is sufficiently large, i.e. if $1/Fr \ll 1$, and both the acceleration in the inertial frame rotating with the turntable and the Coriolis force are negligible if the reduced Reynolds number, $Re = (H_0^2\omega\rho/\mu)^2$, satisfies $Re \ll 1$. Table 2 shows the values of $1/Fr$ and Re for the relevant experiments of FH and SH and demonstrates that both these conditions are reasonably well satisfied for all the experiments considered here.

3. Finite surface tension ($\epsilon = O(1)$)

When $\epsilon = O(1)$ surface-tension effects are significant everywhere. In this case it is not possible to solve (5) analytically, and so we have to use numerical methods to calculate h. In all the numerical calculations presented in this section we restrict ourselves to the case of Greenspan slip, $\lambda = \beta_G/h$, and use the parabolic initial profile $h(r, 0) = h_0(r) = 2(1 - r^2)$. Note that this choice of initial profile satisfies the steady version of (5) in the absence of centripetal effects together with the volume condition (13), and has initial contact angle $\theta(0) = 4$ at $r = 1$.

3.1. *Numerical procedure*

In the case of Greenspan slip we can write (5) as

$$\frac{\partial h}{\partial t} + \frac{f}{3} = 0, \tag{14}$$

where we have introduced

$$f = \frac{1}{r}[rh(h^2 + \beta_G)(q_r + r)]_r, \quad q = \frac{\epsilon^3}{r}(rh_r)_r. \tag{15}$$

In order to implement the numerical procedure we map the unknown domain $0 \leqslant r \leqslant R(t)$ onto the fixed interval $0 \leqslant \xi \leqslant 1$ using the transformation

$$r = R(t)g(\xi). \tag{16}$$

Here g can be any monotonic function such that $g(0) = 0$ and $g(1) = 1$, and by choosing the function $g = g(\xi)$ appropriately we are able to vary the step length in the r-direction and, in particular, concentrate nodes near the contact line $r = R$. The expressions in (15) require the evaluation of h_r/r and q_r/r at $r = 0$. The regularity condition (8) at $r = 0$ means that both h_r and q_r are zero at $r = 0$, and a Maclaurin expansion reveals that $h_r/r = h_{rr}$ and $q_r/r = q_{rr}$ at $r = 0$. With (16) equation (14) becomes

$$\frac{\partial h}{\partial t} - \frac{\dot{R}g}{Rg'}\frac{\partial h}{\partial \xi} + \frac{f}{3} = 0, \tag{17}$$

where $\dot{}\equiv \mathrm{d}/\mathrm{d}t$ and $' \equiv \mathrm{d}/\mathrm{d}\xi$ denote the appropriate derivatives. The r-derivatives in (15) are given by

$$\frac{\partial U}{\partial r} = \frac{1}{Rg'}\frac{\partial U}{\partial \xi}, \quad \frac{\partial^2 U}{\partial r^2} = \frac{1}{(Rg')^2}\left(\frac{\partial^2 U}{\partial \xi^2} - \frac{g''}{g'}\frac{\partial U}{\partial \xi}\right), \tag{18}$$

where U denotes either h or q. In practice, the substitution of (18) into (15) is performed at the programming level; this makes for a more reliable and coherent computer code.

The domain $0 \leqslant \xi \leqslant 1$ is divided into N equally spaced intervals and the derivatives given in (18) are approximated by standard central differences. Equation (17) is differenced in the time coordinate using the Crank–Nicolson method which is not only second-order accurate but also has good stability characteristics; this yields

$$\frac{h_j^{n+1}-h_j^n}{\Delta t}-\frac{g_j}{g_j'}\frac{([\partial h/\partial\xi]_j^{n+1}+[\partial h/\partial\xi]_j^n)}{(R^{n+1}+R^n)}\frac{(R^{n+1}-R^n)}{\Delta t}+\frac{(f_j^{n+1}+f_j^n)}{6}=0 \qquad (19)$$

for $j=1,2,\ldots,N-1$, where h_j^n is the approximation to $h(j\Delta\xi, n\Delta t)$, $\Delta\xi$ and Δt denoting the interval width and time step, respectively. The boundary conditions (8) and (10) are differenced by creating fictitious nodes for $j=-1$ and $j=N+1$ and using central differences. The volume condition (13) becomes

$$2R^2\int_0^1 hgg'\,\mathrm{d}\xi=1, \qquad (20)$$

which is approximated using the trapezoidal rule. Given the numerical solution at time level n, equation (19) and the differenced equations obtained from (8), (10) and (13) form a set of nonlinear equations for the unknowns at time level $n+1$ which are solved using Newton's method. In all the numerical calculations presented in this paper the function g is chosen to be

$$g(\xi)=\frac{\xi}{7+8\chi}[15\chi+(1+\chi)\xi^2(10-3\xi^2)], \qquad (21)$$

which was designed such that $\Delta r(0)/\Delta r(R)=\chi$ (a constant). As expected, in order to obtain solutions for small β_G it is found necessary to use a high concentration of nodes near the contact line $r=R$, and this is achieved with $\chi\gg 1$. For all cases we take $N=200$ with $\chi=100$. Solutions for $0\leqslant t\leqslant 50$ are obtained using a variable time step $\Delta t=\Delta t_0\cosh(n/40)$ for $n=0,1,\ldots,160$ with $\Delta t_0=0.05$. The accuracy of the numerical method is ascertained by comparing the solution with the results at different values of N and Δt_0. Varying N tests the accuracy in the ξ-coordinate and varying Δt_0 the accuracy in the t-coordinate. For all the results the maximum absolute error is less than 10^{-3}.

To obtain some of the results presented in this paper we calculate the value of the dimensional slip coefficient (hereafter denoted by $\hat{\beta}_G$) such that $R(t)$ best fits the appropriate experimental data of FH and SH in a quasi-least-squares sense. This is done as follows. Suppose that the experimentally observed radius is R_i at time t_i for M different observations $i=1,2,\ldots,M$. Let $R(t_i;\hat{\beta}_G)$ be the numerically calculated radius at time t_i using slip coefficient $\hat{\beta}_G$, and define $F(\hat{\beta}_G)$ by

$$F(\hat{\beta}_G)=\sum_{i=1}^{M}[R(t_i;\hat{\beta}_G)-R_i]. \qquad (22)$$

Then choosing $\hat{\beta}_G$ such that $F(\hat{\beta}_G)=0$ gives a quasi-least-squares fit to the data. The solution of $F(\hat{\beta}_G)=0$ is found using the secant rule in which each evaluation of F involves numerically generating a new set of results.

3.2. *Results*

Using the numerical procedure described in § 3.1 we can calculate $h(r,t)$ and hence $R(t)$ for prescribed values of $\hat{\beta}_G$ and, in the first instance, the fixed-contact-angle condition (11), i.e. with θ set equal to its initial value of 4. For example, figure 1(*a*) shows the results for $\epsilon=0.254$ (corresponding to the PDMS4 experimental data) and $\hat{\beta}_G=10^{-9}$. Figure 1(*b*) shows every other profile plotted with $h:r$ in the physically

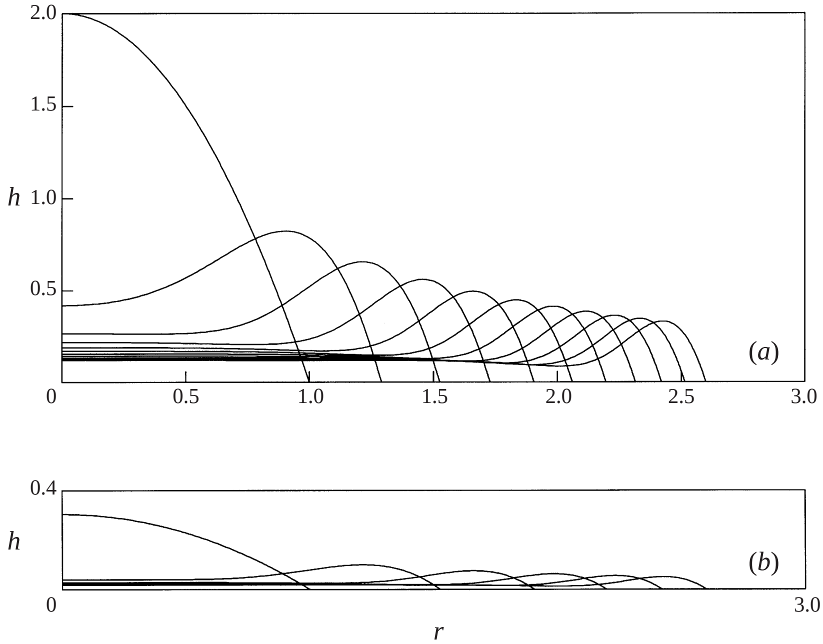

FIGURE 1. (*a*) Numerically calculated free-surface profiles in the case $\epsilon = 0.254$ and $\hat{\beta}_G = 10^{-9}$ for $t = 0, 5, 10, \ldots, 50$ using the fixed-contact-angle condition (11), and (*b*) every other profile plotted with $h : r$ in the physically correct ratio.

		$\kappa\,(\mathrm{m\,s^{-1}})$			
Experiment	$\hat{\beta}_G\,(\mathrm{m^2})$	$\hat{\beta}_G = 10^{-8}$	$\hat{\beta}_G = 10^{-9}$	$\hat{\beta}_G = 10^{-10}$	$\hat{\beta}_G = 10^{-11}$
PDMS1	1.23×10^{-12}	4.06×10^{-4}	6.35×10^{-4}	9.52×10^{-4}	1.81×10^{-3}
PDMS2	1.67×10^{-12}	*b*	6.91×10^{-4}	1.05×10^{-3}	2.18×10^{-3}
PDMS3	*a*	5.10×10^{-5}	6.54×10^{-5}	7.93×10^{-5}	1.02×10^{-4}
PDMS4	1.61×10^{-10}	9.61×10^{-5}	2.57×10^{-4}	*c*	*c*
PDMS5	2.24×10^{-11}	7.61×10^{-5}	1.32×10^{-4}	3.37×10^{-4}	*c*
TCP1	*a*	2.95×10^{-3}	3.23×10^{-3}	3.50×10^{-3}	3.83×10^{-3}
TCP2	*a*	2.15×10^{-3}	2.31×10^{-3}	2.44×10^{-3}	2.59×10^{-3}

TABLE 3. Numerically calculated best-fit values of $\hat{\beta}_G$ (expressed in units of $\mathrm{m^2}$) for the fixed-contact-angle condition (column 2) and numerically calculated best-fit values of κ (expressed in units of $\mathrm{m\ s^{-1}}$) for the Tanner law for four different values of $\hat{\beta}_G$ (columns 3–6) for the experiments of FH (PDMS) and SH (TCP). For *a* the value of $\hat{\beta}_G < 10^{-12}$ required to fit that data is too small for the code to converge. For *b* the numerical algorithm failed to converge and for *c* a value for κ does not exist to fit the data.

correct ratio. In qualitative agreement with the photographs of Melo *et al.* (1989) and SH, the initially parabolic profile flattens in the centre and quickly develops the distinctive capillary-ridge profile near the contact line.

Figure 2 shows the numerically calculated evolution of $R(t)$ with t using the fixed-contact-angle condition (11) for various values of $\hat{\beta}_G$ together with the corresponding experimental results of FH for PDMS1, PDMS2, PDMS4 and PDMS5. In each case

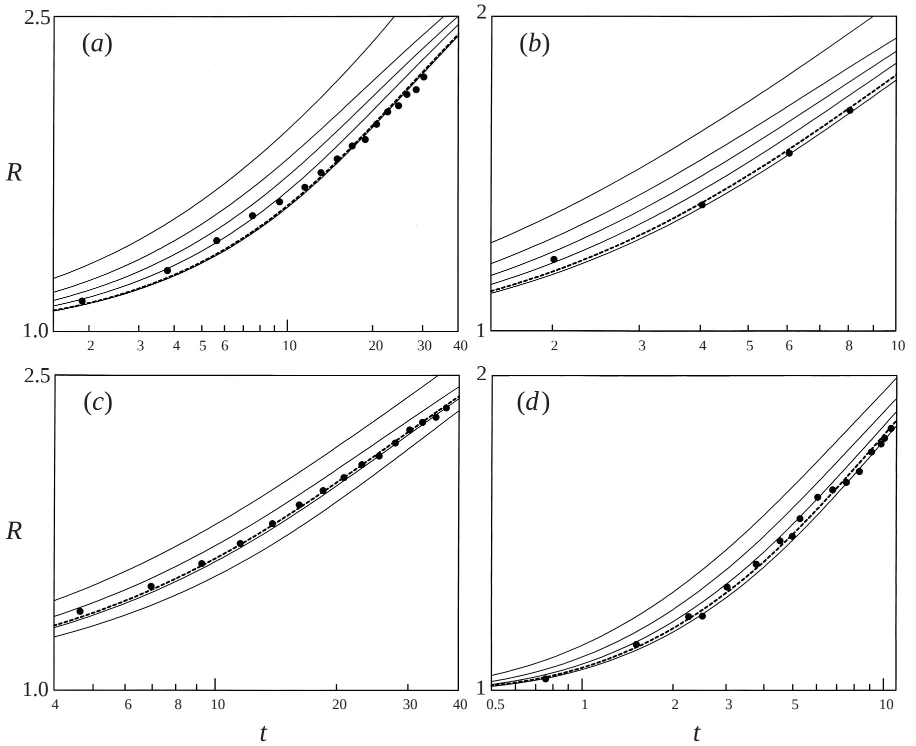

FIGURE 2. Numerically calculated values of $R(t)$ using the fixed-contact-angle condition (11) plotted as functions of t for $\hat{\beta}_G = 10^{-\alpha}$ for $\alpha = 8, 9, 10, 11, 12$ in (*a*) and (*b*) and for $\alpha = 8, 9, 10, 11$ in (*c*) and (*d*) for (*a*) PDMS1, (*b*) PDMS2, (*c*) PDMS4 and (*d*) PDMS5. The filled circles denote the corresponding experimental results of FH. The dashed line denotes the numerically calculated values of $R(t)$ for the value of $\hat{\beta}_G$ that gives the best fit to the experimental data as listed in table 3.

it is possible to choose $\hat{\beta}_G$ to fit the data closely, and so in figure 2 we also show (with the dashed line) the numerically calculated evolution of $R(t)$ with t for the value of $\hat{\beta}_G$ that gives the best fit to the experimental data, calculated using the procedure described in § 3.1. The values of $\hat{\beta}_G$ obtained in this way for the different experiments are shown in table 3. In each case the fit is an excellent one since the solutions for $R(t)$ capture both the gradient and curvature of the experimental results. We emphasize that this is not simply a curve-fitting exercise: in each case there is only the single free parameter $\hat{\beta}_G$, and the evolution of $R(t)$ with t is then determined from the numerical solution of (5). In the other three cases, namely PDMS3, TCP1 and TCP2, the present numerical calculations failed to converge, requiring a value of $\hat{\beta}_G < 10^{-12}$.

We now consider the situation when the fixed-contact-angle condition (11) is replaced by the Tanner law (12). In this case we have the additional dimensional

FIGURE 3. Numerically calculated values of $R(t)$ using the Tanner law (12) plotted as functions of t for $\kappa = 10^{-1}, 10^{-2}, \ldots, 10^{-5}$ (solid curves with 10^{-1} at the top and 10^{-5} at the bottom) with $\hat{\beta}_G = 10^{-9}$ for (*a*) PDMS1, (*b*) PDMS2, (*c*) PDMS3, (*d*) PDMS4, (*e*) PDMS5, (*f*) TCP1 and (*g*) TCP2. The filled circles denote the corresponding experimental results of FH or SH, as appropriate. The dashed line denotes the numerically calculated values of $R(t)$ for the value of κ that gives the best fit to the experimental data as listed in table 3.

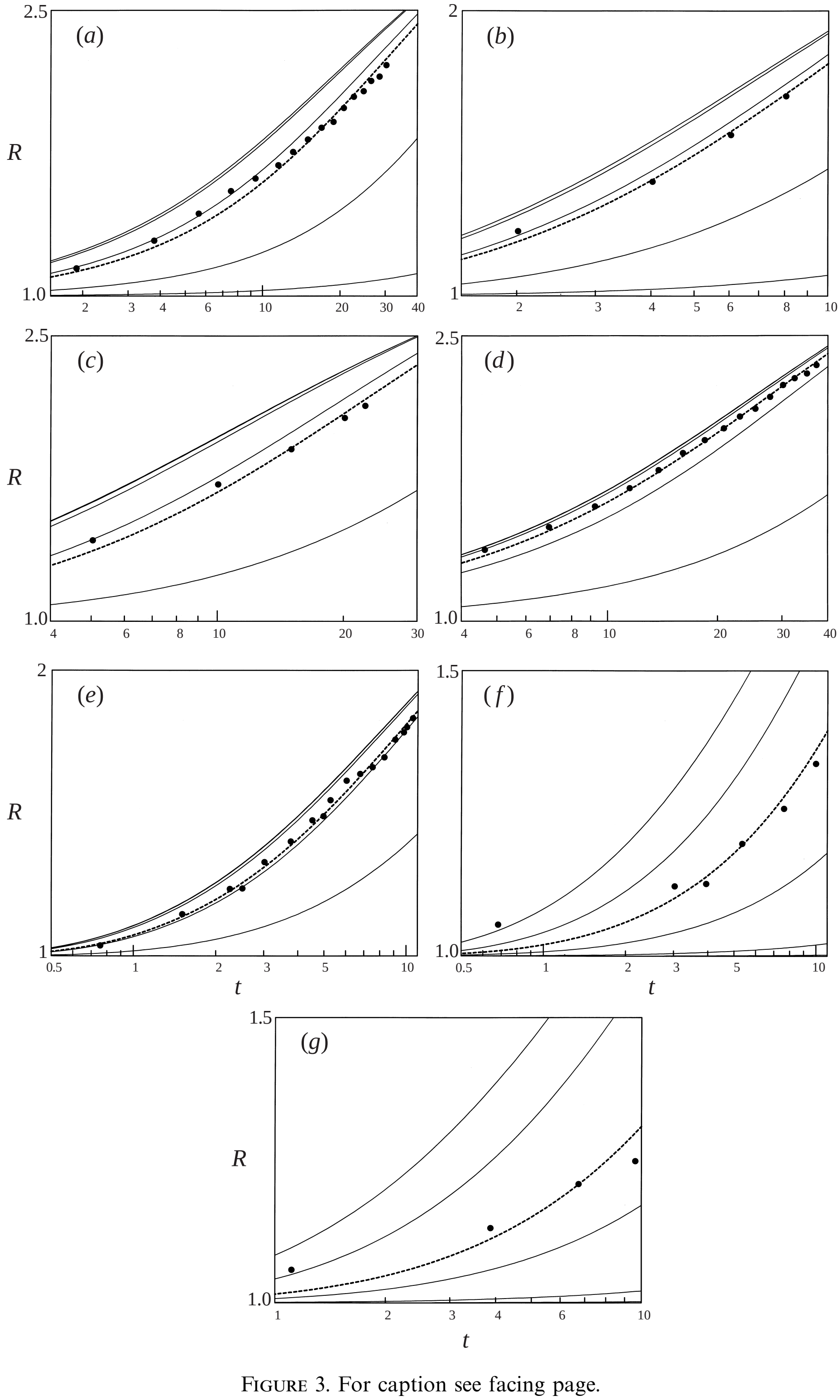

FIGURE 3. For caption see facing page.

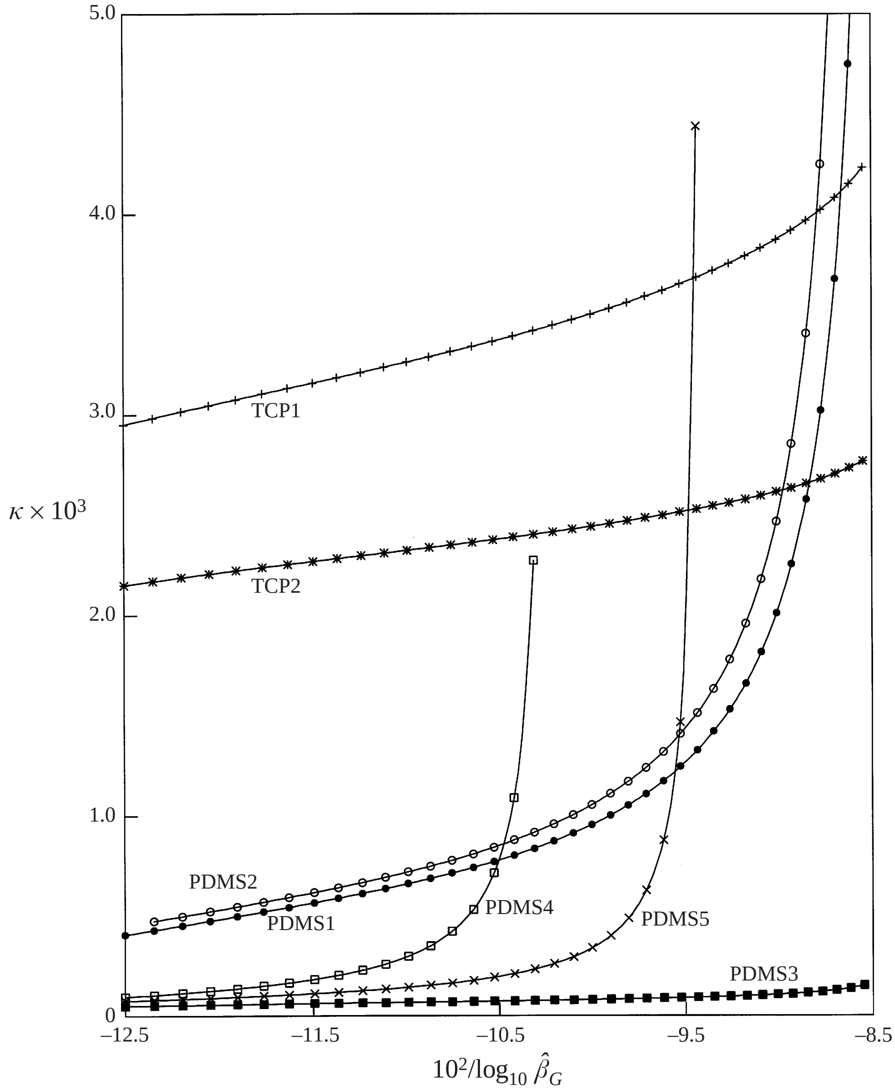

FIGURE 4. Best-fit values of κ for the four substances PDMS1/2, PDMS3, PDMS4/5 and TCP1/2 plotted as functions of $10^2/\log_{10}\hat{\beta}_G$.

parameter κ, and hence each set of results is characterized by three parameters ϵ, $\hat{\beta}_G$ and κ. Thus for a given ϵ and $\hat{\beta}_G$ it is possible to select the value of κ that best fits the experimental data using an algorithm similar to that used to find $\hat{\beta}_G$ for the fixed-contact-angle case. Figure 3 shows the numerically calculated evolution of $R(t)$ with t for $\hat{\beta}_G = 10^{-9}$ for various values of κ and (with the dashed line) the evolution for the value of κ that gives the best fit to the experimental data for all seven of the experiments considered here. The best-fit values of κ for various $\hat{\beta}_G$ are shown in table 3. These cover a wide range of values, which is as expected since the physical constants of the substances used in the experiments differ widely. From table 3 it is evident that, as expected, when the experiments involve the same substance (namely PDMS1/PDMS2, PDMS4/PDMS5 and TCP1/TCP2) the predicted values of κ are not dissimilar from each other. The numerically calculated best-fit values of κ for all the different experiments are plotted as functions of $10^2/\log_{10}\hat{\beta}_G$ in figure 4. Evidently these curves are approximately linear provided that $\hat{\beta}_G$ is not too small (the precise range depending on the particular experiment), in agreement with the theoretical predictions.

Since all the values of ϵ appropriate to the experiments listed in table 2 satisfy the condition $\epsilon \ll 1$ reasonably well, it is natural to ask whether the numerical results presented above can be captured by either the solution in the case $\epsilon = 0$ or the leading-order asymptotic solution in the limit $\epsilon \to 0$, and so in § 4 and § 5 we examine these solutions in detail.

4. No surface tension ($\epsilon = 0$)

In the case $\epsilon = 0$ surface-tension effects are absent from the problem and (5) reduces to simply

$$h_t + \frac{1}{3r}[r^2h^2(h+\lambda)]_r = 0, \tag{23}$$

a first-order nonlinear hyperbolic equation which can be solved exactly using the method of characteristics. In this section we describe the solutions of (23) in the cases of no slip, a uniform precursor layer, the Navier slip model and the Greenspan slip model respectively. Note that in this case the solutions are uniquely determined by specifying the initial condition (7), and satisfy (8) and (13) identically; they do not, in general, satisfy the boundary condition (10) with either (11) or (12) at any contact line that may be present.

In most of the cases described in detail below, parts of the free-surface profile steepen and the free surface eventually becomes triple valued (like a breaking wave). Clearly in this situation the lubrication approximation fails; however these solutions are still of interest because, if interpreted correctly, they provide the outer solution in the asymptotic limit $\epsilon \to 0$ described in § 5.

4.1. *Solution in the case of no slip* ($\lambda = 0$)

The exact solution of (23) in the case of no slip at the substrate ($\lambda = 0$) was first obtained by Emslie *et al.* (1958), and can be written most conveniently in the parametric form

$$r = r_0(h_0)\left(1 + \frac{4h_0^2 t}{3}\right)^{3/4}, \quad h = h_0\left(1 + \frac{4h_0^2 t}{3}\right)^{-1/2}, \tag{24}$$

where $r_0 = r_0(h_0)$ is the initial profile of the drop. In particular, this solution predicts that if the initial profile has a contact line then both the contact angle and the position of the contact line remain fixed at their initial values as the drop evolves. The free-surface profile becomes vertical if $\mathrm{d}r/\mathrm{d}r_0 = 0$ and so the free surface becomes triple valued for the first time at $t = t_c$ if t_c, defined to be the minimum value of

$$-\frac{3}{2h_0}\left(2h_0 + 3r_0\frac{\mathrm{d}h_0}{\mathrm{d}r_0}\right)^{-1}, \tag{25}$$

is positive.

Figure 5(*a*) shows the evolution of the parabolic initial profile $h_0(r_0) = 2(1 - r_0^2)$ calculated using (24), and demonstrates that the effect of rotation is to flatten rapidly the 'upper' free surface of the drop. (Corresponding results for other initial profiles

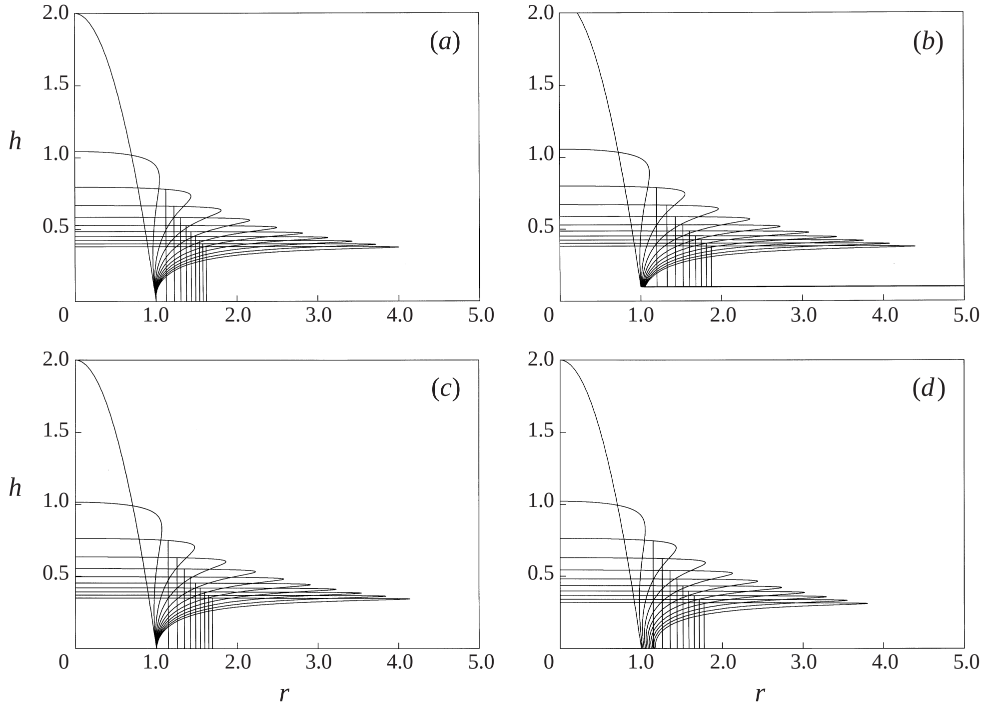

FIGURE 5. Evolution of a spreading drop in the case of (*a*) no slip calculated using (24), (*b*) no slip and a uniform precursor layer with $\delta_0 = 1/10$ calculated using (24), (*c*) Navier slip with $\beta_N = 1/10$ calculated using (31) and (*d*) Greenspan slip with $\beta_G = 1/10$ calculated using (33) at $t = 0, 0.5, \ldots, 5$. In each case the initial profile is $h_0(r_0) = 2(1 - r_0^2)$ except for (*b*) when it is $h_0(r_0) = 2(1 - r_0^2)\mathrm{H}(1 - r_0^2) + \delta_0$. The vertical lines mark $r = r_F$ and meet the profiles at the points (r_F, h_F).

are given by Emslie *et al.* 1958 and Momoniat & Mason 1998.) In this case breaking first occurs when $t = t_c = 1/3$ at

$$r = r_c = \frac{5^{5/4}}{8} \approx 0.9346, \quad h = h_c = \frac{3\sqrt{5}}{10} \approx 0.6708, \tag{26}$$

in agreement with the results shown in figure 5(*a*).

A particularly simple solution can be obtained for the case of a uniform initial profile given by $h_0(r_0) = \mathrm{H}(1 - r_0^2)$, where $\mathrm{H}(\cdot)$ is the unit Heaviside function. In this case (24) yields simply

$$r = r_0\left(1 + \frac{4t}{3}\right)^{3/4}, \quad h = \left(1 + \frac{4t}{3}\right)^{-1/2}. \tag{27}$$

4.2. *Solution in the case of a uniform precursor layer*

Emslie *et al.*'s (1958) solution also applies to an initial profile that includes a precursor layer of uniform thickness $\delta = \delta(t)$. In particular, the uniform thickness of the precursor layer with initial thickness $\delta(0) = \delta_0$ is given by

$$\delta(t) = \delta_0\left(1 + \frac{4\delta_0^2 t}{3}\right)^{-1/2}. \tag{28}$$

Figure 5(*b*) shows the evolution of the initial profile $h_0(r_0) = 2(1 - r_0^2)\mathrm{H}(1 - r_0^2) + \delta_0$

calculated using (24) in the case $\delta_0 = 1/10$. In this case breaking first occurs when

$$t = t_c = \frac{4}{3}\frac{1}{(2+\delta_0)^2} \approx 0.3023 < \frac{1}{3} \tag{29}$$

at

$$r = r_c = \frac{5^{5/4}\sqrt{2}\,(2+\delta_0)^{1/2}}{16} \approx 0.9577, \quad h = h_c = \frac{3\sqrt{5}\,(2+\delta_0)}{20} \approx 0.7044. \tag{30}$$

Note that the effect of the precursor layer is always to hasten breaking relative to the case $\delta_0 = 0$.

4.3. *Solution in the case of Navier slip* ($\lambda = \beta_N$)

Yanagisawa (1987) presented some numerical solutions to (23) in the case of Navier slip but, in fact, the exact solution can be obtained in the parametric form

$$r = r_0(h_0)\left(\frac{1+\mathrm{W}(x)}{1+\mathrm{W}(x_0)}\right)^{3/2}\left(\frac{\mathrm{W}(x_0)}{\mathrm{W}(x)}\right)^{1/2}, \quad h = -\frac{\beta_N}{1+\mathrm{W}(x)}, \tag{31}$$

where

$$x = x_0 \exp\left(-\frac{2\beta_N^2 t}{3}\right), \quad x_0 = -\left(1+\frac{\beta_N}{h_0}\right)\exp\left[-\left(1+\frac{\beta_N}{h_0}\right)\right], \tag{32}$$

and where $\mathrm{W} = \mathrm{W}(x)$ denotes the 'lower' real branch of Lambert's W function which satisfies $\mathrm{W}\exp(\mathrm{W}) = x$. Details of the derivation of this solution and of Lambert's W function are given in the Appendix. As in the no-slip case, this solution predicts that if the initial profile has a contact line then both the contact angle and the position of the contact line remain fixed at their initial values as the drop evolves.

Figure 5(*c*) shows the evolution of the initial profile $h_0(r_0) = 2(1 - r_0^2)$ calculated using (31) in the case $\beta_N = 1/10$. In this case a straightforward numerical evaluation of the condition $\mathrm{d}r/\mathrm{d}r_0 = 0$ shows that breaking first occurs when $t = t_c \approx 0.3223 < 1/3$ at $r = r_c \approx 0.9420$ and $h = h_c \approx 0.6491$. Note that the effect of the slip is to hasten breaking relative to the case $\beta_N = 0$.

4.4. *Solution in the case of Greenspan slip* ($\lambda = \beta_G/h$)

The exact solution of (23) in the case of Greenspan slip was obtained by Tu (1987), and can be written in the parametric form

$$\left.\begin{aligned} r &= r_0(h_0)\exp\left(-\frac{2\beta_G t}{3}\right)\left[\left(1+\frac{h_0^2}{\beta_G}\right)\exp\left(\frac{4\beta_G t}{3}\right) - \frac{h_0^2}{\beta_G}\right]^{3/4}, \\ h &= h_0\left[\left(1+\frac{h_0^2}{\beta_G}\right)\exp\left(\frac{4\beta_G t}{3}\right) - \frac{h_0^2}{\beta_G}\right]^{-1/2}. \end{aligned}\right\} \tag{33}$$

The position of the contact line is given by $R(t) = \exp(\beta_G t/3)$ and the contact angle by $\theta = \theta(0)\exp(-\beta_G t)$, and so it is interesting to note that in this case the relationship between the contact angle and the contact-line speed can be expressed as a rather unusual Tanner law in the form

$$R_t = \frac{\beta_G}{3}\left(\frac{\theta}{\theta(0)}\right)^{-1/3}. \tag{34}$$

The free-surface profile becomes vertical for the first time at $t = t_c$ if t_c, defined to be the minimum value of

$$-\frac{3}{4\beta_G}\log\left[\frac{2\beta_G + h_0\left(2h_0 + 3r_0\,\mathrm{d}h_0/\mathrm{d}r_0\right)}{h_0\left(2h_0 + 3r_0\,\mathrm{d}h_0/\mathrm{d}r_0\right)}\right], \tag{35}$$

is positive.

Figure 5(*d*) shows the evolution of the initial profile $h_0(r_0) = 2(1 - r_0^2)$ calculated using (33) in the case $\beta_G = 1/10$. In this case breaking first occurs when

$$t = t_c = -\frac{3}{4\beta_G}\log\left(1 - \frac{4\beta_G}{9}\right) \approx 0.3410 > \frac{1}{3} \tag{36}$$

at

$$r = r_c = \frac{5^{5/4}\sqrt{3}}{8(9 - 4\beta_G)^{1/4}} \approx 0.9453, \quad h = h_c = \frac{\sqrt{5}\,(9 - 4\beta_G)^{1/2}}{10} \approx 0.6557. \tag{37}$$

Note that the effect of the slip is always to delay breaking relative to the case $\beta_G = 0$, and indeed prevent it altogether if $\beta_G > \beta_{G_c} = 9/4$.

5. The asymptotic limit of weak surface tension ($\epsilon \to 0$)

In the asymptotic limit of weak surface tension, $\epsilon \to 0$, surface-tension effects are significant only where the spatial gradients of h are sufficiently large. However, as we have already seen, even a simple parabolic initial profile can develop just such a region of rapid variation prior to becoming triple valued. Once this has happened the location of the inner region in which surface-tension effects are significant is obtained by truncating the outer (no-surface-tension) solution at an appropriate position $r = r_F(t)$ (where $h = h_F(t)$) such that the volume of fluid under the upper surface of the truncated profile is equal to the initial volume of the drop, i.e. r_F is given by

$$2\int_0^{r_F} (h - \delta) r\,\mathrm{d}r = 1. \tag{38}$$

In the case of a uniform precursor layer the leading-order asymptotic solution in the inner region was analysed by Troian *et al.* (1989) and uniformly valid leading-order composite solutions were obtained by Moriarty *et al.* (1991). Here we note that the inner region is narrow on the scale of the outer problem (specifically, it has width $O(\epsilon)$) and so the lubrication approximation remains valid only provided that $A_0 \ll \epsilon$ (or equivalently $Ca^{1/3} \ll 1$), a more restrictive condition than that in the outer region. Inspection of the values in table 2 indicates that this condition is barely satisfied for the present experiments, suggesting (as our subsequent results will show) that the asymptotic solution in the limit $\epsilon \to 0$ may not be appropriate in these cases.

Substituting the solution in the case of no slip given in (24) into (38) and changing the variable of integration from r to h_0 yields the condition

$$2\int_{h_{0M}}^{h_{0F}} \left[\left(1 + \frac{4h_0^2 t}{3}\right)\frac{\mathrm{d}r_0}{\mathrm{d}h_0}(h_0) + 2th_0 r_0(h_0)\right] h_0 r_0(h_0)\,\mathrm{d}h_0 = 1, \tag{39}$$

where h_{0F} and h_{0M} are the values of h_0 corresponding to $h = h_F$ at $r = r_F$ and $h = h_M$ at $r = 0$, respectively.

In the case $h_0(r_0) = 2(1 - r_0^2)$ (in which case $h_{0M} = 2$) equation (39) implies that

$$\frac{2th_{0F}^2}{3}\left(h_{0F}^2 - 2h_{0F} + \frac{3}{8t}\right) = 0, \tag{40}$$

and so provided that $t \geqslant 3/8$ the appropriate solution for h_{0F} is

$$h_{0F} = 1 + \left(1 - \frac{3}{8t}\right)^{1/2}. \tag{41}$$

Now r_F and h_F can be evaluated directly from (24) to yield the explicit expressions

$$\begin{aligned} r_F(t) &= 2^{-1/2}6^{-3/4}\left[1 - \left(1 - \frac{3}{8t}\right)^{1/2}\right]^{1/2}\left[3 + 16t + 16t\left(1 - \frac{3}{8t}\right)^{1/2}\right]^{3/4}, \\ h_F(t) &= 6^{1/2}\left[1 + \left(1 - \frac{3}{8t}\right)^{1/2}\right]\left[3 + 16t + 16t\left(1 - \frac{3}{8t}\right)^{1/2}\right]^{-1/2}. \end{aligned} \tag{42}$$

In particular, these expressions yield

$$r_F = \left(\frac{3^3}{2^5}\right)^{1/4} \approx 0.9584, \quad h_F = \left(\frac{2}{3}\right)^{1/2} \approx 0.8165 \tag{43}$$

at $t = 3/8$, and

$$\begin{aligned} r_F &= \left(\frac{4t}{3}\right)^{1/4} + \frac{1}{16}\left(\frac{4t}{3}\right)^{-3/4} + O(t^{-7/4}), \\ h_F &= \left(\frac{4t}{3}\right)^{-1/2} - \frac{1}{8}\left(\frac{4t}{3}\right)^{-3/2} + O(t^{-5/2}) \end{aligned} \tag{44}$$

as $t \to \infty$.

In the case $h_0(r_0) = \mathrm{H}(1 - r_0^2)$ equation (27) trivially yields

$$r_F = \left(1 + \frac{4t}{3}\right)^{1/4}, \quad h_F = \left(1 + \frac{4t}{3}\right)^{-1/2}. \tag{45}$$

Evidently this solution coincides with that in (44) at leading (but not higher) order in the limit $t \to \infty$.

If the parabolic initial profile is modified to include a uniform precursor layer $\delta = \delta(t)$ then the modified version of (40) determining h_{0F} is

$$\left(1 - \frac{h_{0F} - \delta_0}{2}\right)\left(1 + \frac{4h_{0F}^2 t}{3}\right)^{3/2}(h_F - \delta) + \delta_0\left(1 + \frac{\delta_0}{4}\right) + h_{0F}\left(\frac{h_{0F}}{4} - \frac{\delta_0}{2} - 1\right) = 0, \tag{46}$$

and explicit expressions for r_F and h_F can be obtained by substituting the appropriate value of $h_0 = h_{0F}$ into (24). These expressions are omitted for brevity. In the limit $t \to \infty$ we have $h_{0F} \sim c$, where the appropriate solution for the constant c is given by

$$c = \tfrac{1}{2}(2 - \delta_0 + [(2 + \delta_0)(2 + 5\delta_0)]^{1/2}), \tag{47}$$

and hence

$$r_F \sim \left(1 - \frac{c - \delta_0}{2}\right)^{1/2}\left(\frac{4c^2 t}{3}\right)^{3/4}, \quad h_F \sim \left(\frac{4t}{3}\right)^{-1/2}. \tag{48}$$

Thus in the limit $\delta_0 \to 0$ the coefficient of $t^{3/4}$ in the asymptotic expansion of r_F is

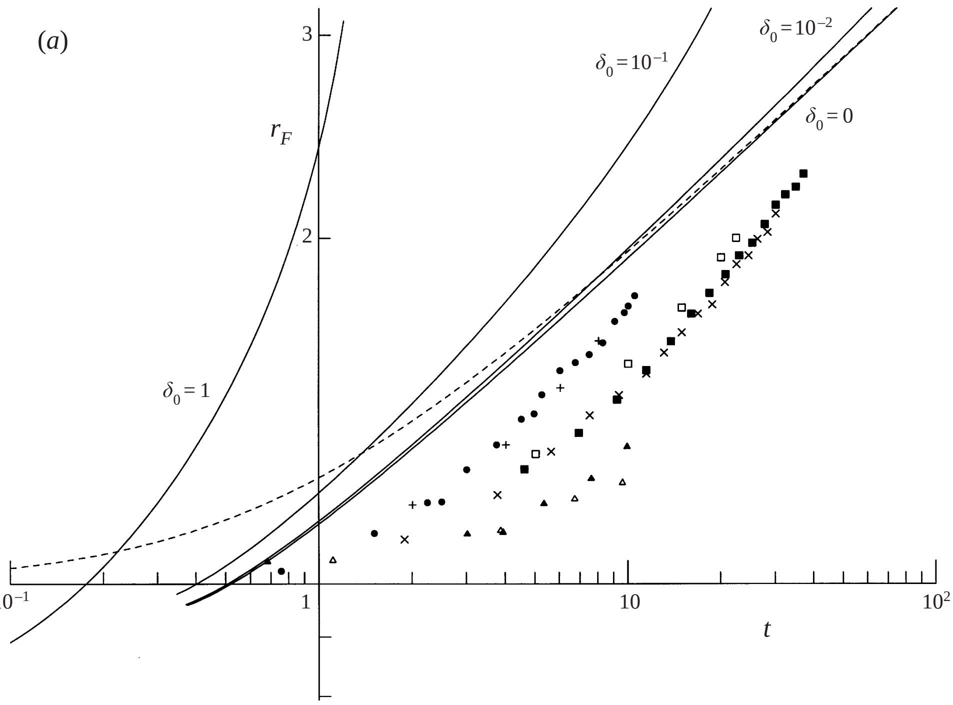

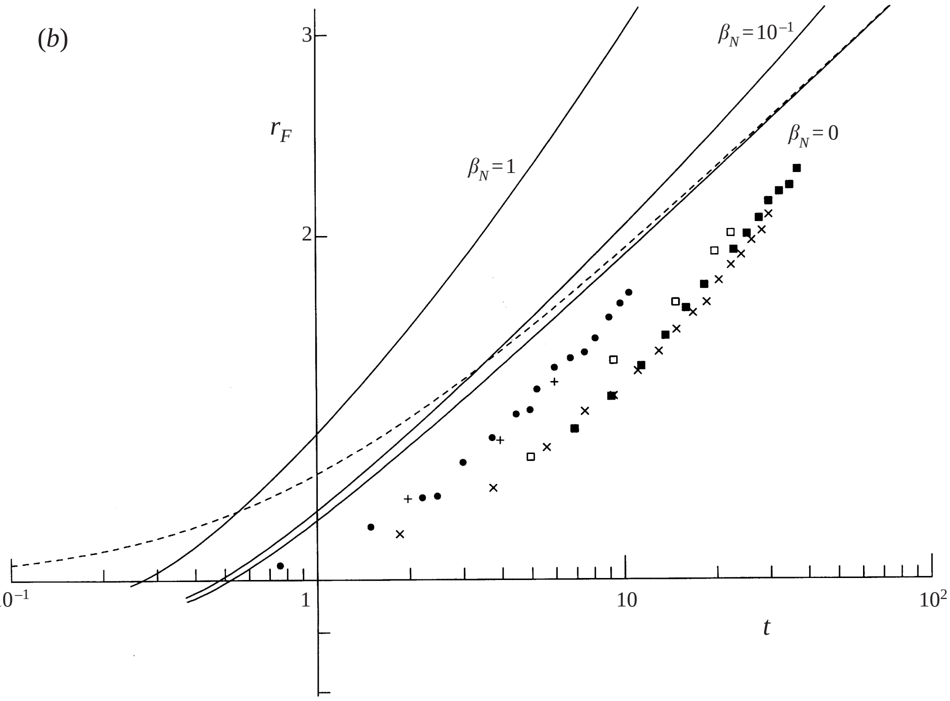

FIGURE 6. For caption see facing page.

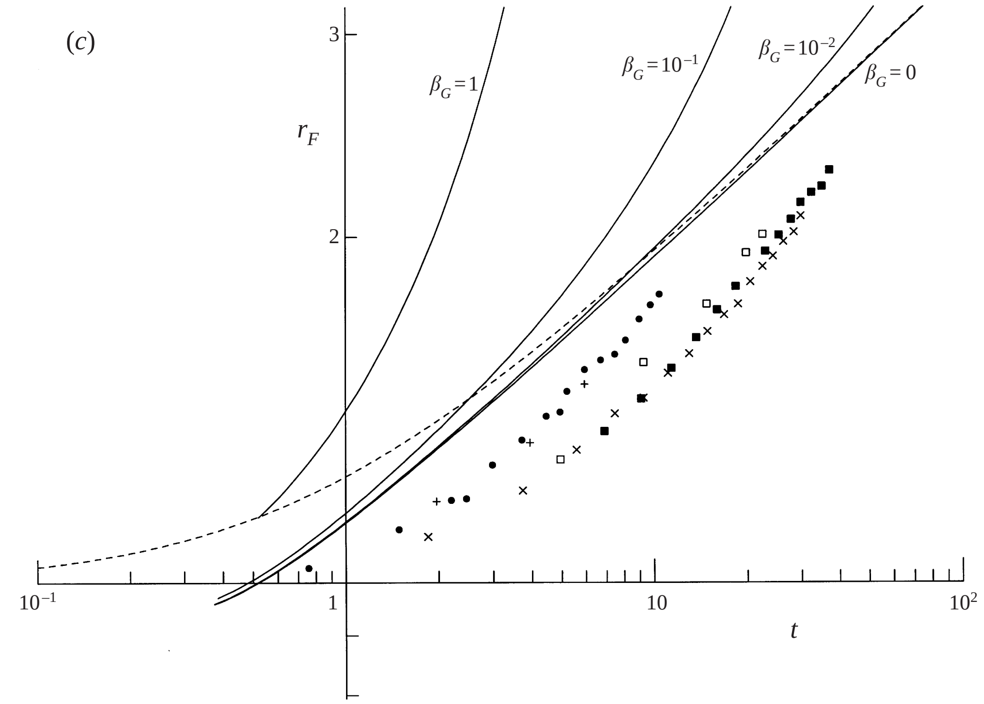

FIGURE 6. Numerically calculated values of r_F plotted as a function of t for a range of values of (*a*) the initial thickness of the uniform precursor layer, δ_0, (*b*) the Navier slip coefficient, β_N, and (*c*) the Greenspan slip coefficient, β_G, for a parabolic initial profile. The dashed line denotes the corresponding values of r_F calculated using the solution of Emslie *et al.* (1958) for a uniform initial profile with the same volume (given by (45)). The experimental data for both PDMS and TCP from FH and SH respectively are also shown and are denoted as follows: PDMS1 (cross), PDMS2 (plus), PDMS3 (open square), PDMS4 (filled square), PDMS5 (filled circle), TCP1 (filled triangle) and TCP2 (open triangle).

given by $4\delta_0 3^{-3/4} + O(\delta_0^2)$. In particular, comparison of (48) with (44) shows that the effect of the precursor layer is to make the leading-order large-time behaviour of r_F (but not h_F) totally different from that in the case $\delta_0 = 0$.

We have been unable to evaluate the integral in (38) analytically for the case of Navier slip using the solution given in (31). Numerical results will be presented subsequently. However, we can make analytical progress for the case of Greenspan slip; in this case use of the solution given in (33) for the parabolic initial profile yields

$$\frac{2Th_{0F}^2}{3}\left(h_{0F}^2 - 2h_{0F} + \frac{3}{8T}\right) = 0, \tag{49}$$

in place of (40), where we have defined

$$T = \frac{3}{4\beta_G}\left[1 - \exp\left(-\frac{4\beta_G t}{3}\right)\right]. \tag{50}$$

Thus provided that $T \geqslant 3/8$ (which is possible only if $\beta_G < 2$) the appropriate solution for h_{0F} is

$$h_{0F} = 1 + \left(1 - \frac{3}{8T}\right)^{1/2}. \tag{51}$$

Explicit expressions for r_F and h_F can be obtained by substituting $h_0 = h_{0F}$ into (33). Again these expression are omitted for brevity, but one may show that they yield

$$r_F = \frac{3^{1/2}}{2}\left(\frac{3}{2-\beta_G}\right)^{1/4}, \quad h_F = \left(\frac{2-\beta_G}{3}\right)^{1/2} \tag{52}$$

when $T = 3/8$, and $h_{0F} \sim [2 + (4 - 2\beta_G)^{1/2}]/2$ and hence

$$\left.\begin{aligned} r_F &\sim \tfrac{1}{2}[2-(4-2\beta_G)^{1/2}]^{1/2}\left[\frac{4+\beta_G+2(4-2\beta_G)^{1/2}}{2\beta_G}\right]^{3/4}\exp\left(\frac{\beta_G t}{3}\right), \\ h_F &\sim \tfrac{1}{2}[2+(4-2\beta_G)^{1/2}]\left[\frac{2\beta_G}{4+\beta_G+2(4-2\beta_G)^{1/2}}\right]^{1/2}\exp\left(-\frac{2\beta_G t}{3}\right) \end{aligned}\right\} \tag{53}$$

as $t \to \infty$. In particular, comparison of (53) with (44) shows that the effect of Greenspan slip is to make the leading-order large-time behaviour of both r_F and h_F totally different from that in the case $\beta_G = 0$.

In figure 6 we plot typical numerically calculated examples of r_F as a function of t for the uniform precursor, Navier slip and Greenspan slip solutions for the parabolic initial profile. Each part of figure 6 also shows the corresponding values of r_F calculated using the Emslie *et al.* (1958) solution for both parabolic and uniform initial profiles (given by (42) and (45) respectively) and the experimental data for both PDMS and TCP from FH and SH respectively. Note that the numerically calculated results in figure 6 are in agreement with the appropriate exact and asymptotic results presented above. In particular, the results in figure 6 show that in all three cases (precursor layer, Navier slip and Greenspan slip) the effect of increasing the relevant parameter (δ_0, β_N and β_G respectively) from zero is always to increase the value of r_F at time t (where it is defined) relative to its value in the case of no slip. Furthermore, since all the experimental data clearly lie well below the no-slip solution it is evidently impossible to choose parameter values so that any of these solutions can reproduce these particular experimental results. Thus in order to do this we must abandon the asymptotic limit $\epsilon \to 0$ and return to the numerically calculated solutions for the general case of weak but finite values of ϵ presented in § 3.

6. Conclusions

The combination of analytical and numerical work presented in the present paper reveals several new insights into our understanding of the practically important spin-coating process.

In § 4 and § 5 we described the solutions to several spin-coating problems (involving either a slip model or a uniform precursor layer), both in the case of no surface tension and in the asymptotic limit of weak surface tension. We obtained analytical and numerical solutions for the profile of the drop, and in particular the evolution of the radius of the drop, $R(t)$, as a function of time, in the limit of weak surface tension. At the end of § 5 we compared these results with the experimental measurements of FH and SH. Rather unexpectedly we found that, although the experimentally measured values of ϵ are indeed smaller than unity and the asymptotic solutions do indeed capture many of the qualitative features of the experimental results, they cannot give quantitative agreement with the experimental results for the evolution of $R(t)$. In order to achieve qualitative agreement we had to include weak but finite surface-tension effects, and in order to do this we had to obtain numerical solutions to the problem. Our numerical procedure and results were described in § 3. In particular, we found that using the Greenspan slip model we could achieve excellent agreement between numerical and experimental results for the evolution of $R(t)$. Interestingly we also found that both a fixed-contact-angle condition and a specific Tanner law are capable of reproducing the experimental results well.

The major outstanding question still to be addressed is the prediction of the critical radius (or alternatively the critical time) for the onset of instability. Hopefully now that the evolution of the drop up to the onset of instability has been accurately reproduced numerically it should be possible to calculate the critical conditions for the onset of instability and compare them with the experimental results now available in the literature.

Part of this work was carried out while one of the authors (S. K. W.) was a Visiting Scholar in the Department of Engineering Science and Applied Mathematics of Northwestern University where he was partially supported under a United States Department of Energy Grant in the Basic Energy Sciences while he was visiting Professor S. G. Bankoff and Professor S. H. Davis. The authors wish to thank Professor S. H. Davis (Northwestern University) for his insightful comments and Professor G. M. Homsy (Stanford University) for providing them with a copy of the original figure 10 of the paper by Fraysse & Homsy (1994) from which much of the experimental data used in the present work was taken. In addition the authors gratefully acknowledge the encouragement given to them by Professor D. M. Sloan (University of Strathclyde) to undertake the present work.

Appendix. Derivation of the exact solution of (23) in the case of Navier slip ($\lambda = \beta_N$)

In this Appendix we describe the derivation of the exact solution of (23) in the case of Navier slip, $\lambda = \beta_N$. On a characteristic we have

$$\frac{\mathrm{d}h}{\mathrm{d}t} = \frac{\partial h}{\partial t} + \frac{\partial h}{\partial r}\frac{\mathrm{d}r}{\mathrm{d}t}, \tag{A 1}$$

and so the characteristic equations for (23) are given by

$$\frac{\mathrm{d}h}{\mathrm{d}t} = -\frac{2h^2}{3}(h + \beta_N), \tag{A 2}$$

$$\frac{\mathrm{d}r}{\mathrm{d}t} = \frac{rh}{3}(3h + 2\beta_N). \tag{A 3}$$

Integrating (A 2) yields

$$\left[\log\left(1 + \frac{\beta_N}{h}\right) - \frac{\beta_N}{h}\right]_{h_0}^{h} + \frac{2\beta_N^2 t}{3} = 0. \tag{A 4}$$

Lambert's W function $\mathrm{W} = \mathrm{W}(x)$ is defined to be a solution of $\mathrm{W}\exp(\mathrm{W}) = x$. There are infinitely many complex branches of $\mathrm{W}(x)$, but for the present purpose we can restrict our attention to the real branches of $\mathrm{W}(x)$ shown in figure 7. These consist of a monotonically increasing 'upper' branch defined on $[-1/\mathrm{e}, \infty)$ and satisfying $\mathrm{W}(-1/\mathrm{e}) = -1$ and $\mathrm{W}(x) \sim \log(x)$ as $x \to \infty$, and a monotonically decreasing 'lower' branch defined on $[-1/\mathrm{e}, 0)$ and satisfying $\mathrm{W}(-1/\mathrm{e}) = -1$ and $\mathrm{W}(x) \sim \log(-x)$ as

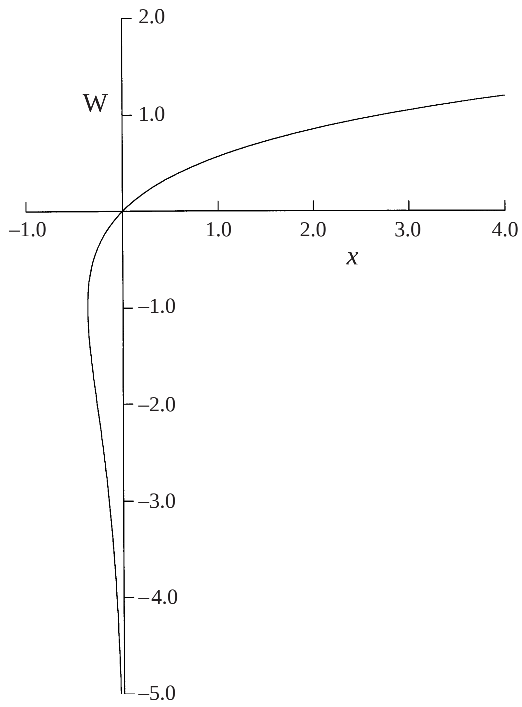

FIGURE 7. The real branches of Lambert's W function, W = W(x).

$x \to 0^-$. If we write

$$x = x_0 \exp\left(-\frac{2\beta_N^2 t}{3}\right), \quad x_0 = -\left(1+\frac{\beta_N}{h_0}\right)\exp\left[-\left(1+\frac{\beta_N}{h_0}\right)\right], \tag{A 5}$$

then (A 4) can be solved explicitly for h in terms of W(x) to yield

$$h = -\frac{\beta_N}{1+\mathrm{W}(x)}, \tag{A 6}$$

where in this equation and hereafter we restrict our attention to values of W(x) on the lower branch (which by definition always satisfy $\mathrm{W}(x) \leqslant -1$ and hence correspond to physically realistic solutions with $h \geqslant 0$). Note that from the definition of x_0 we have

$$\mathrm{W}(x_0) = -\left(1+\frac{\beta_N}{h_0}\right), \tag{A 7}$$

and so (A 6) does indeed satisfy the initial condition $h = h_0$ at $t = 0$. Substituting the solution for h given in (A 6) into (A 3) yields

$$\log\left(\frac{r}{r_0}\right) = \frac{\beta_N^2}{3}\int_0^t \frac{3}{(1+\mathrm{W}(x))^2} - \frac{2}{1+\mathrm{W}(x)}\,\mathrm{d}t. \tag{A 8}$$

Using the definition of x given in (A 5) and the identities

$$\int \frac{\mathrm{d}x}{x(1+\mathrm{W}(x))} = \log|\mathrm{W}(x)|, \tag{A 9}$$

$$\int \frac{\mathrm{d}x}{x(1+\mathrm{W}(x))^2} = \log\left|\frac{\mathrm{W}(x)}{1+\mathrm{W}(x)}\right|, \tag{A 10}$$

we can evaluate the integrals in (A 8) to yield

$$\log\left(\frac{r}{r_0}\right) = \left[\tfrac{3}{2}\log|1+\mathrm{W}(x)| - \tfrac{1}{2}\log|\mathrm{W}(x)|\right]_0^t, \qquad (\mathrm{A}\,11)$$

and hence

$$r = r_0(h_0)\left(\frac{1+\mathrm{W}(x)}{1+\mathrm{W}(x_0)}\right)^{3/2}\left(\frac{\mathrm{W}(x_0)}{\mathrm{W}(x)}\right)^{1/2}. \qquad (\mathrm{A}\,12)$$

In the limit $h_0 \to 0$ we have $h \sim h_0$ and $r \sim r_0(h_0)$, and so both the contact angle and the position of the contact line remain fixed at their initial values for all values of t. Note that in the limit $\beta_N \to 0$ equations (A 6) and (A 12) reduce to the familiar solutions in the case of zero slip given in (24).

REFERENCES

Anderson, D. M. & Davis, S. H. 1995 The spreading of volatile liquid droplets on heated surfaces. *Phys. Fluids* **7**, 248–265.

Bertozzi, A. L. & Brenner, M. P. 1997 Linear stability and transient growth in driven contact lines. *Phys. Fluids* **9**, 530–539.

Braun, R. J., Murray, B. T., Boettinger, W. J. & McFadden, G. B. 1995 Lubrication theory for reactive spreading of a thin drop. *Phys. Fluids* **7**, 1797–1810.

Brenner, M. P. 1993 Instability mechanism at driven contact lines. *Phys. Rev.* E **47**, 4597–4599.

Duffy, B. R. & Wilson, S. K. 1997 A third-order differential equation arising in thin-film flows and relevant to Tanner's law. *Appl. Math. Lett.* **10**, 63–68.

Emslie, A. G., Bonner, F. T. & Peck, L. G. 1958 Flow of a viscous liquid on a rotating disk. *J. Appl. Phys.* **29**, 858–862.

Ehrhard, P. 1994 The spreading of hanging drops. *J. Colloid Interface Sci* **168**, 242–246.

Ehrhard, P. & Davis, S. H. 1991 Non-isothermal spreading of liquid drops on horizontal plates. *J. Fluid Mech.* **229**, 365–388.

Fraysse, N. & Homsy, G. M. 1994 An experimental study of rivulet instabilities in centrifugal spin coating of viscous Newtonian and non-Newtonian fluids. *Phys. Fluids* **6**, 1491–1504 (referred to herein as FH).

Greenspan, H. P. 1978 On the motion of a small viscous droplet that wets a surface. *J. Fluid Mech.* **84**, 125–143.

Hocking, L. M. 1983 The spreading of a thin drop by gravity and capillarity. *Q. J. Mech. Appl. Maths* **36**, 55–69.

Hocking, L. M. 1992 Rival contact-angle models and the spreading of drops. *J. Fluid Mech.* **239**, 671–681.

Hocking, L. M. 1994 The spreading of drops with intermolecular forces. *Phys. Fluids* **6**, 3224–3228.

Huppert, H. E. 1982 Flow and instability of a viscous current down a slope. *Nature* **300**, 427–429.

Larson, R. G. & Rehg, T. G. 1997 Spin coating. In *Liquid Film Coating* (ed. S. F. Kistler & P. M. Schweizer), pp. 709–734. Chapman Hall.

López, P. G., Bankoff, S. G. & Miksis, M. J. 1996 Non-isothermal spreading of a thin liquid film on an inclined plane. *J. Fluid Mech.* **324**, 261–286.

López, P. G., Miksis, M. J. & Bankoff, S. G. 1997*a* Stability and evolution of a dry spot. *Northwestern University Applied Mathematics Tech. Rep.* 9605 (July 1997).

López, P. G., Miksis, M. J. & Bankoff, S. G. 1997*b* Inertial effects on contact line instability in the coating of a dry inclined plate. *Phys. Fluids* **9**, 2177–2183.

McKinley, I. S., Wilson, S. K. & Duffy, B. R. 1999 Spin coating and air-jet blowing of thin viscous drops. *Phys. Fluids* **11**, 30–47.

Melo, F., Joanny, J. F. & Fauve, S. 1989 Fingering instability of spinning drops. *Phys. Rev. Lett.* **63**, 1958–1961.

Momoniat, E. & Mason, D. P. 1998 Investigation of the effect of the Coriolis force on a thin fluid film on a rotating disk. *Intl J. Non-Linear Mech.* **33**, 1069–1088.

MORIARTY, J. A., SCHWARTZ, L. W. & TUCK, E. O. 1991 Unsteady spreading of thin liquid films with small surface tension. *Phys. Fluids* A **3**, 733–742.

ORON, A., DAVIS, S. H. & BANKOFF, S. G. 1997 Long-scale evolution of thin liquid films. *Rev. Mod. Phys.* **69**, 931–980.

SHIKHMURZAEV, Y. D. 1997*a* Moving contact lines in liquid/liquid/solid systems. *J. Fluid Mech.* **334**, 211–249.

SHIKHMURZAEV, Y. D. 1997*b* Spreading of drops on solid surfaces in a quasi-static regime. *Phys. Fluids* **9**, 266–275.

SPAID, M. A. & HOMSY, G. M. 1996 Stability of Newtonian and viscoelastic dynamic contact lines. *Phys. Fluids* **8**, 460–478.

SPAID, M. A. & HOMSY, G. M. 1997 Stability of viscoelastic dynamic contact lines: an experimental study. *Phys. Fluids* **9**, 823–832 (referred to herein as SH).

TROIAN, S. M., HERBOLZHEIMER, E., SAFRAN, S. A. & JOANNY, J. F. 1989 Fingering instabilities of driven spreading films. *Europhys. Lett.* **10**, 25–30.

TU, Y.-O 1987 Contact line slippage of fluid flow on a rotating disk. *J. Colloid Interface Sci.* **116**, 237–240.

WILSON, S. K. & DUFFY, B. R. 1998 On the gravity-driven draining of a rivulet of viscous fluid down a slowly varying substrate with variation transverse to the direction of flow. *Phys. Fluids* **10**, 13–22.

WILSON, S. K. & TERRILL, E. L. 1996 The dynamics of planar and axisymmetric holes in thin fluid layers. In *First European Symposium on The Mechanics of Thin Film Coatings, Leeds University, 19–22 September 1995* (ed. P. H. Gaskell, M. D. Savage & J. L. Summers), pp. 288–297. World Scientific.

YANAGISAWA, M. 1987 Slip effect for thin liquid film on a rotating disk. *J. Appl. Phys.* **61**, 1034–1037.

YOUNG, G. W. 1994 Mathematical description of viscous free surface flows. In *Free Boundaries in Viscous Flows* (ed. R. A. Brown & S. H. Davis), pp. 1–27. Springer.